
FROM SPECTRA TO BIOPHYSICAL INSIGHTS: END-TO-END LEARNING WITH A BIASED RADIATIVE TRANSFER MODEL

Yihang She^{*1}, Clement Atzberger^{†2}, Andrew Blake^{‡1,2}, and Srinivasan Keshav^{§1}

¹University of Cambridge

²Mantle Labs

ABSTRACT

Advances in machine learning have boosted the use of Earth observation data for climate change research. Yet, the interpretability of machine-learned representations remains a challenge, particularly in understanding forests’ biophysical reactions to climate change. Traditional methods in remote sensing that invert radiative transfer models (RTMs) to retrieve biophysical variables from spectral data often fail to account for biases inherent in the RTM, especially for complex forests. We propose to integrate RTMs into an auto-encoder architecture, creating an end-to-end learning approach. Our method not only corrects biases in RTMs but also outperforms traditional techniques for variable retrieval like neural network regression. Furthermore, our framework has potential generally for inverting biased physical models. The code is available on <https://github.com/yihshe/ai-refined-rtm.git>.

1 INTRODUCTION

Over the last few decades, satellite remote sensing has made a vast amount of Earth observation data available (Claverie et al., 2018). However, traditional statistical learning approaches in ML are unable to yield interpretable representations (Chen et al., 2016) which restricts their applications. In the context of climate change, one significant example concerns understanding the biophysical variables of forests and their response to climate threats (Thompson et al., 2009), for example: leaf area index, pigmentation, and crown coverage, all of which have direct implications on ecosystem resilience or susceptibility to climate change.

Physical models, such as Radiative Transfer Models (RTMs) (Rosema et al., 1992), have been developed to simulate canopy-radiation interactions and open pathways for retrieving biophysical variables from satellite spectra. Classical approaches for inverting RTMs include numerical optimization (Goel, 1988), look-up tables (Combal et al., 2003), and neural network regressions (Gong, 1999) which is regarded as the state-of-the-art. Despite decades of research, the complexity of forest structures leads to discrepancies between simulated and measured spectra — biases that significantly affect the accuracy of estimated biophysical variables using classical approaches (Widlowski et al., 2013). Inverting RTMs is challenging also due to the correlations of variables and the ill-posed nature of the inversion problem.

To tackle these challenges, we propose an end-to-end approach to learning biophysical variables from satellite spectra while simultaneously correcting the systematic biases of the RTM. Deviating from traditional methods, we draw inspiration from physics-informed machine learning (Lu et al., 2020; Zérah et al., 2022; Hao et al., 2022) and disentangled representation learning (Eastwood & Williams, 2018; Locatello et al., 2019).

^{*}ys611@cam.ac.uk

[†]clement@mantle-labs.com

[‡]ab@ablake.ai

[§]sk818@cam.ac.uk

Specifically, we use an auto-encoder architecture, training the encoder to predict RTM variables based on input spectra. The RTM is integrated as the decoder, with additional non-linear layers to correct the systematic bias (Fig. 1). Once trained, the encoder component can be used independently to extract more accurate biophysical variables from forest spectra, and the bias correction module can be used to generate more realistic forest signatures.

Our contributions can be summarised as follows:

- We have developed an end-to-end learning approach with a complex physical model to retrieve biophysical variables from satellite spectral data.
- By incorporating a bias correction layer, we have effectively corrected the bias, resulting in our model’s learned variables outperforming state-of-the-art methods for variable retrieval.
- Our methodology for inverting the RTM has broader implications for inverting biased physical models.

2 RELATED WORK

2.1 DISENTANGLED REPRESENTATION LEARNING

Disentangled representation learning aims to uncover lower dimensional and semantically meaningful factors of variation from high-dimensional data (Locatello et al., 2019). Our approach to inferring biophysical variables by inverting a physical model is partly related to previous work on analysis-by-synthesis for faces: Active Shape Models (Cootes et al., 1995) iteratively refine pose, scale, and shape parameters, progressively minimizing the loss between the observed data and the output of a “Point Distribution Model”. However, where those approaches compute each application of the inverse, we seek to learn the inverse function itself, represented as a neural network.

State-of-the-art methods for unsupervised learning of disentangled representations often use the Variational Autoencoder (VAE) (Kingma & Welling, 2013) and its variants e.g. β -VAE (Higgins et al., 2017). VAE approaches are based on probabilistic modeling (Locatello et al., 2019) and allow disentangled variables to emerge from learning (Kumar et al., 2018). Alternatively, Generative Adversarial Networks (GAN) (Goodfellow et al., 2020) have also shown success in learning interpretable and disentangled representations for image synthesis, for example InfoGAN (Chen et al., 2016) and StyleGAN (Karras et al., 2019). However, as generative models, disentangled variables usually emerge only from learning and they lack an effective inference mechanism (citekumar2018variational).

For physical models however, as here, the situation is simplified in that the forward model is deterministic and benefits from having a predetermined set of interpretable variables, namely the physical input parameters to the model. Therefore, we use a neural auto-encoder architecture to learn an inverse function that directly predicts disentangled biophysical variables from input spectra.

2.2 PHYSICS-INFORMED MACHINE LEARNING

Methods combining physical knowledge with machine learning vary depending on problem context and physical constraint representation (Hao et al., 2022). Inverse problems represent a popular paradigm within this field, aiming to infer physical parameters from data while satisfying given physical constraints. In these approaches, auto-encoders usually serve as the base of the physics-informed architecture, where a known physical model acts as a fixed decoder and the model learns a complementary encoder as the inverse. For instance, Lu et al. (2020) apply a VAE-based architecture to predict latent parameters controlling the dynamics of a system governed by partial differential equations. Similarly, Zérah et al. (2022) introduce “pheno-VAE” to extract the phenological parameters from NDVI time series, which also uses VAE-based architecture with a temporal model as the decoder, describing the shape of the time series. While pheno-VAE is one of the few attempts to deal with remote sensing data, the inverse is taken to be simply a double-logistic function, making the inversion process quite straightforward. In contrast, our approach accommodates the more complex physical models often needed to explain remote sensing data, and hence also for analysing such data.

2.3 CANOPY REFLECTANCE MODELS AND INVERSION

Canopy reflectance models simulate spectral bidirectional forest reflectance given the inputs of important forest characteristics (Widlowski et al., 2013). There are four main types of canopy models, namely: geometrical models (Li & Strahler, 1985), analytical models e.g. RTMs (Suits, 1971), hybrids of geometrical and analytical models (Atzberger, 2000), and ray-tracing models (Gastellu-Etchegorry et al., 1996). Ray-tracing offers accuracy but at the cost of increased computational complexity, which limits its feasibility for model inversion. The model we study in the project is the Invertible Forest Reflectance Model (INFORM) Atzberger (2000), which is a hybrid combining both geometrical models and RTM. INFORM can simulate a more realistic relationship between canopy and reflectance, while striking a balance between model complexity and computational efficiency, well-suited for inverse problems.

Classical approaches to invert RTMs include numerical optimizations (Goel, 1988), look-up tables (Combal et al., 2003) and neural network regression (Gong, 1999; Schlerf & Atzberger, 2006). However, none of these methods consider the systematic bias that a fixed RTM typically exhibits, owing to its only approximate representation of a given physical system.

We do not claim originality in using an auto-encoder to invert physical models — this concept has been investigated as above and, more recently, specifically for RTMs (Zérah et al., 2023). However, we highlight that systematic bias is a critical factor affecting the quality of variables retrieved from RTMs. Our contribution, that we believe to be original, is to combine an auto-encoder with a bias correction network, to significantly improve inverse computation. Furthermore, we introduce a comprehensive framework that seamlessly incorporates complex physical models into an end-to-end learning pipeline, encompassing model conversion, forward pass implementation, and backpropagation. This is applicable quite generally to computing an inverse function for a given fixed physical models with bias correction included. In that way, in addition to obtaining the inverse function, the original model is also bias corrected.

3 METHODS

3.1 INFORM AND VARIABLES TO LEARN

To test our proposed approach with forestry applications we use the INFORM model (Atzberger, 2000). INFORM consists of a group of sub-models to model the reflectance of forest canopies at different levels. Each sub-model has a set of input parameters describing the biophysical and geometric features of the canopy components (Tab. 1). We aim to invert INFORM to estimate certain biophysical variables within known ranges (Tab. 1). We fix other variables at typical values for the study area. Crown diameter cd and canopy height h are derived from fractional coverage fc using allometric equations (Jucker et al., 2017).

The uncertainties in a physical model can be classified into three categories: aleatory, which is inherent to probabilistic models; epistemic, stemming from insufficient knowledge of model parameters; and ontological, resulting from model incompleteness. The bias we seek to mitigate arises from the ontological uncertainty of the model. Specifically, the RTM exhibits bias due to incomplete forest modeling, necessitated by simplified assumptions in representing canopy-radiation interactions. Consequently, detecting and correcting such biases is crucial for accurate biophysical variable retrieval.

3.2 END-TO-END LEARNING WITH INFORM

To incorporate an RTM such as INFORM into an end-to-end learning pipeline, it must be made fully differentiable. However, like many other RTMs, INFORM is implemented using Numpy arrays and operations — it is sufficient for the use to create a lookup table or to create a synthetic dataset for neural network regression — however, it has no definitions on how derivatives should be calculated for each operation. Thus it is necessary to reimplement INFORM using a machine learning framework such as PyTorch, which can track the computational graph and enable backpropagation. Differentiability is crucial for integrating physical models into machine learning workflows. For example, Loper & Black (2014) developed a renderer in Chumpy that facilitates differentiable rendering, eliminating the need for manual derivative computations.

Table 1: **The biophysical variables used by INFORM.** Variables can be attributed to three hierarchical levels. Seven variables will be inferred directly. * **Note** that cd will be inferred from fc based on their geometric relationship and h will be inferred from cd using an allometric equation derived from the database compiled by Jucker et al. (2017) (see Appendix A.4).

Group	Variable	Acronym	To infer	Default Value	Sample Range	
					Min	Max
Background	Soil brightness factor	psoil	✗	0.8	-	-
	Structure Parameter	N	✓	-	1	3
Leaf Model	Chlorophyll A+B	cab	✓	-	10	80
	Water Content	cw	✓	-	0.001	0.02
	Dry Matter	cm	✓	-	0.005	0.05
	Carotenoids	car	✗	10	-	-
	Brown Pigments	cbrown	✗	0.25	-	-
	Anthocyanins	anth	✗	2	-	-
	Proteins	cp	✗	0.0015	-	-
	Carbon-based Constituents	cbc	✗	0.01	-	-
		Leaf Area Index	LAI	✓	-	0.01
Canopy Model	Leaf Angle Distribution	typeLIDF	✗	Beta Distribution	-	-
	Hot Spot Size	hspot	✗	0.01	-	-
	Observation Zenith Angle	tto	✗	0	-	-
	Sun Zenith Angle	tts	✗	30	-	-
	Relative Azimuth Angle	psi	✗	0	-	-
Forest Model	Undergrowth LAI	LAIu	✓	-	0.01	1
	Stem Density	sd	✗	500	-	-
	Fractional Coverage	fc	✓	-	0.1	1
	Tree Height	h	✓*	-	-	-
	Crown Diameter	cd	✓*	-	-	-

However, INFORM is a complicated physical model, and reimplementing it in PyTorch line by line seems challenging. In light of the recent development of large language models, we decide to utilize GPT-4 (OpenAI, 2023) to assist in the conversion from Numpy to PyTorch. GPT-4 is useful for converting commonly seen operations from NumPy into PyTorch. With its assistance, we have successfully converted 1,742 lines of code across various scripts, from the original implementation, into PyTorch (see Appendix A.1 for details).

As a physical model, input variables of INFORM carry specific physical meanings and are inherently non-negative in real-world scenarios, as outlined in Tab. 1. Providing input variables outside their defined value ranges can result in failure during the forward pass. For instance, the structure parameter N acts as a denominator in some calculations, and setting it to 0 will cause computational errors and result in infinite numerical values in the simulated spectra. To mitigate these issues, we employ a Sigmoid function to learn a scaling factor for each input variable, ensuring the factor ranges between 0 and 1. Subsequently, we rescale these normalized factors to their respective known ranges as specified in Tab. 1 (see Appendix A.3.2 for more details). This process not only guarantees that the output of INFORM remains meaningful and within expected bounds but also narrows the search space for biophysical parameters. By adjusting input variables to avoid improbable ranges, we enhance the model’s reliability in the forward pass and ensure a more effective search for the inversion process.

The steps so far should have obtained a fully differentiable INFORM. In practice, modelling the canopy-radiation interaction needs exponential, logarithm, and square root functions which can lead to numerically unstable derivative computations. An effective workaround ensures the optimization process bypasses instability points during backpropagation to allow continuous convergence (see Appendix A.3.3 and Appendix A.3.4).

These combined measures enable the integration of a complex physical model like INFORM into an end-to-end learning pipeline. Our approach to converting INFORM into PyTorch, including our designs for the forward pass and backpropagation process, could be generalized to incorporate other physical models into machine learning pipelines.

Table 2: **Sentinel-2 bands** to use. *VNIR stands for Visible and Near Infrared. SWIR stands for Short Wave Infrared.*

Band	B2	B3	B4	B5	B6	B7	B8	B8a	B9	B11	B12
Resolution	10 m	10 m	10 m	20 m	20 m	20 m	10 m	20 m	60 m	20 m	20 m
Central Wavelength	490 nm	560 nm	665 nm	705 nm	740 nm	783 nm	842 nm	865 nm	940 nm	1610 nm	2190 nm
Description	Blue	Green	Red	VNIR	VNIR	VNIR	VNIR	VNIR	SWIR	SWIR	SWIR

3.3 DATASET

The real dataset we are using (denoted by D_r) consists of 17962 individual spectra (denoted by $X_r = \{x_{r,1}, \dots, x_{r,N}\}$) extracted from 1283 individual sites across Austria. Samples of D_r are extracted from each site as a temporal sequence covering April to October 2018 — both coniferous and deciduous forests, consisting of 12 species. X_r consists of 11 bands used to retrieve biophysical variables. Collecting ground truth data for biophysical variables is largely impractical. Therefore, the interpretation of results has to rely on plausibility checks — on variable distributions and temporal evolution patterns. We use available prior knowledge of tree species and temporal data to validate our model’s biophysical estimates. For example, LAI inferred from a given site’s spectra should exhibit distinct and repeatable temporal trends.

3.4 INVERTING THE RTM

To learn biophysical variables from satellite spectra, we use an auto-encoder (AE) architecture extended with bias correction layers to train an encoder that maps measured spectra to biophysical variables. We replace the decoder of the AE with INFORM (Fig. 1), in order to correct the systematic bias of INFORM while refining the learning of biophysical variables (see appendix for training details).

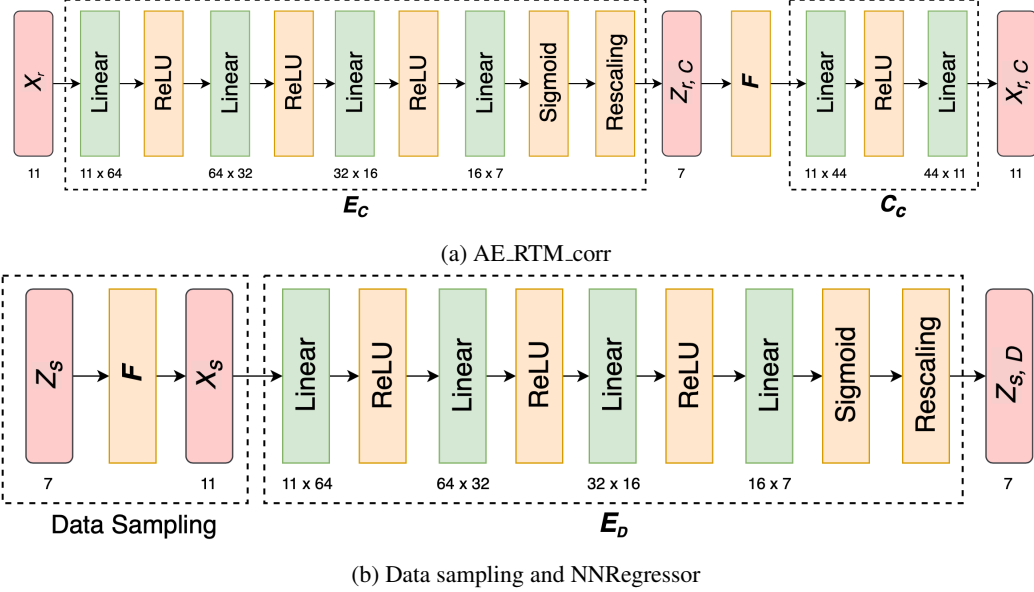


Figure 1: **Learning the inverse.** (a) End-to-end learning of the inverse E_C of RTM F together with bias correction function C_C . (b) Classical approach — sampling D_s to train regressive neural network E_D — serves as a baseline.

A classical auto-encoder consists of an encoder E_A and a decoder D_A (eq. (1)).

$$X_{r,A} = D_A(E_A(X_r)) \quad (1)$$

By replacing D_A in eq. (1) with INFORM (denoted by F), we ensure that the encoder (denoted by E_B) will embed X_r as biophysical variables $Z_{r,B}$ (eq. (2)), which are then passed to F to reconstruct

spectra $X_{r,B}$ (eq. (3)).

$$Z_{r,B} = \mathbf{E}_B(X_r) \quad (2)$$

$$X_{r,B} = \mathbf{F}(\mathbf{E}_B(X_r)) \quad (3)$$

The final model, AE_RTM_corr, has additional non-linear layers \mathbf{C}_C (eq. (4)) to correct the systematic bias of \mathbf{F} .

$$X_{r,C} = \mathbf{C}_C(\mathbf{F}(\mathbf{E}_C(X_r))) \quad (4)$$

3.5 BASELINE

We have sampled a synthetic dataset $D_s = \{Z_s, X_s\}$ using INFORM, following Tab. 1. D_s consists of sampled variables Z_s and synthetic spectra X_s . Using D_s , we train a neural network regression model “NNRegressor” replicating the classical approach to inverting the RTM (Gong, 1999). NNRegressor (model architecture denoted by \mathbf{E}_D) is first trained on D_s and then evaluated on the test set of D_r to predict $Z_{r,D}$ given X_r . To get the spectral reconstruction $X_{r,D}$, $Z_{r,D}$ will be passed to \mathbf{F} .

3.6 IMPLEMENTATION DETAILS

Both D_r and D_s are further split into the train, validation, and test sets, where samples from the same individual site are placed in the same set to avoid data leakage. All input data are standardized before training. For model training, the batch size is 64. We use the Adam optimizer and set the initial learning rate as 1e-3 and weight decay as 1e-4. The training loss is mean squared error (MSE). The maximum number of epochs is 100, the learning rate is reduced by a factor of 10 after 50 epochs, and training stops if the MSE loss on the validation set does not improve after an additional 10 epochs. We use 11 spectral bands excluding B1 and B10 to allow fair comparison, as these two bands are not available in D_r .

4 RESULTS

4.1 BIAS CORRECTION

The systematic bias of INFORM can be observed by comparing X_r with $X_{r,D}$ based on the $Z_{r,D}$ that is inferred by NNRegressor (Tab. 3). The distributions of the learned biases display distinct patterns among forest types (Fig. 2). The RTM tends to under-estimate the spectral components for deciduous forest but over-estimate for coniferous forest. Per-band analysis (Fig. 3) indicates overestimation in the visible bands at lower ranges and underestimation in the near-infrared bands at higher ranges, with less pronounced bias in the shortwave bands. Reconstruction loss with AE_RTM_corr is more than an order of magnitude lower than with NNRegressor (Tab. 3).

Table 3: **MSE loss of trained models evaluated on D_r .** *The Mean Squared Error (MSE) of AE_RTM_corr is more than an order of magnitude lower than NNRegressor.*

Model	Architecture	Dataset	MSE_{train}	MSE_{val}	MSE_{test}
AE_RTM_corr	$\mathbf{E}_C + \mathbf{F} + \mathbf{C}_C$	D_r	0.0210	0.0235	0.0217
NNRegressor	\mathbf{E}_D	D_r	-	-	0.6676

4.2 BIOPHYSICAL VARIABLES

The variables retrieved by our model follow a unimodal distribution (Fig. 4b), whereas NNRegressor distorts the distribution of most variables to boost extreme values (Fig. 4a), tending to break out of the preset parameter ranges. We clustered the variables inferred by our model, by forest type (Fig. 4b). Coniferous and deciduous forests have distinct distributions aligned with their respective attributes. Examining the co-distributions of variables, LAI displays apparent positive correlation with cw and negative correlation with $LAIu$ under AE_RTM_corr (Fig. 5), while the variables learned by NNRegressor do not retain these correlation patterns. This makes sense as higher LAI reduces light penetration causing lower plant growth in the understory, hence lower $LAIu$.

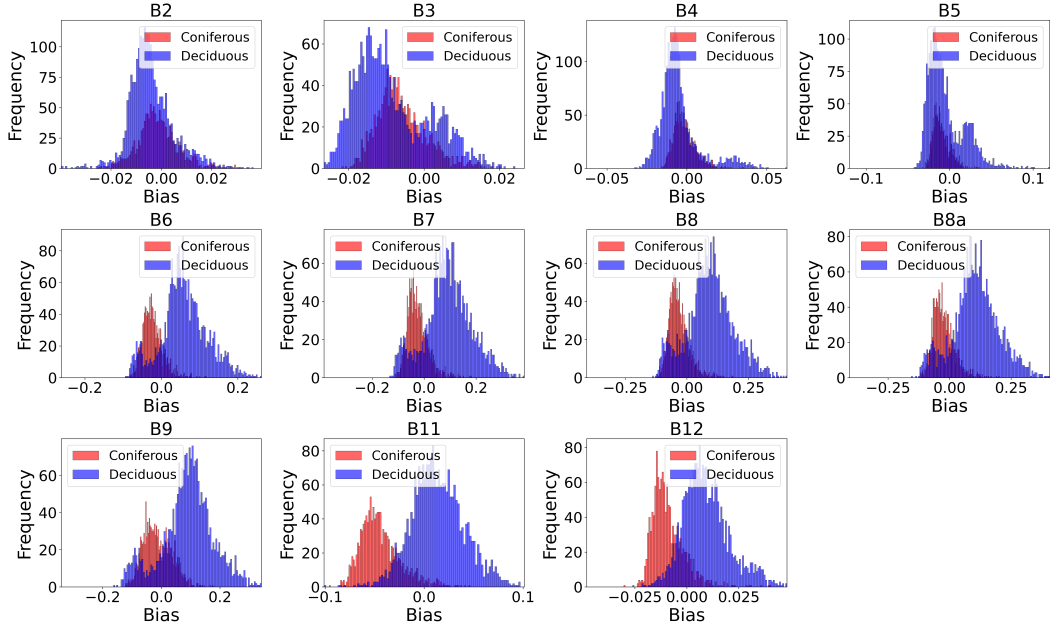
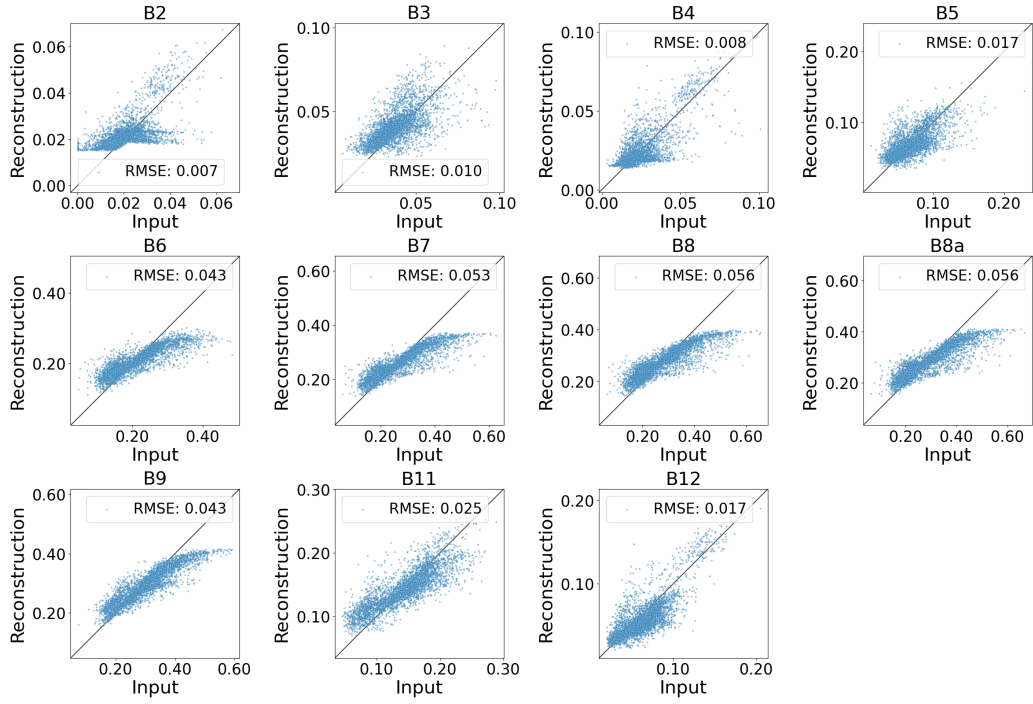


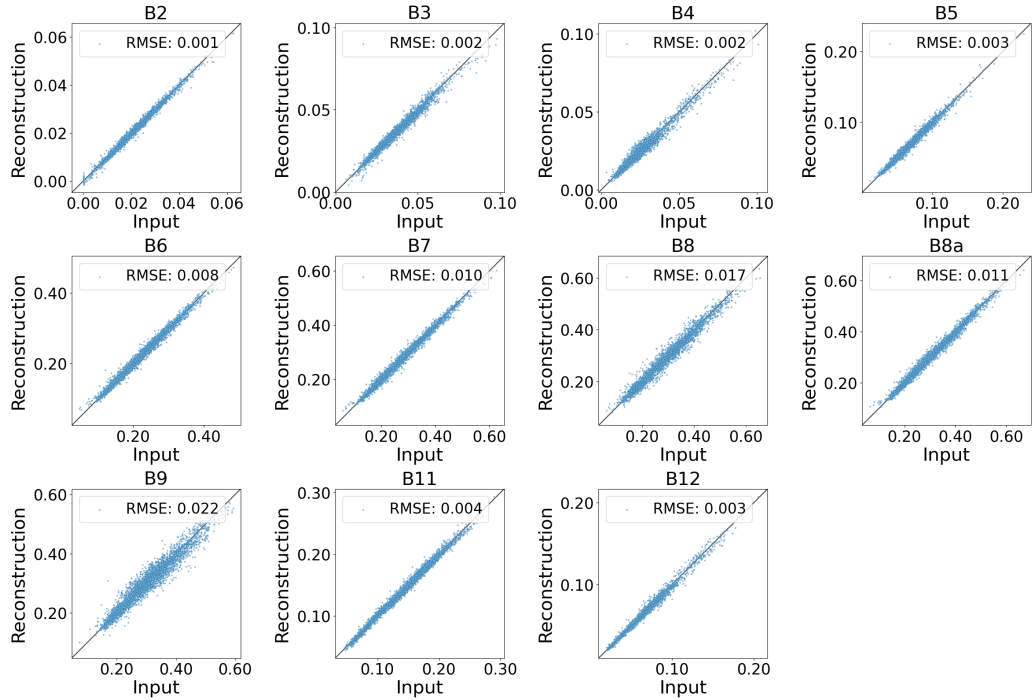
Figure 2: **Distributions of biases learned by AE_RTM_corr.** The biases are computed by subtracting the corrected spectra from the originally simulated spectra, given the same set of inferred variables. For bands in the near-infrared and short wave ranges, the RTM tends to under-estimate the spectra for deciduous forest but over-estimate for coniferous forest.

Next, comparing temporal variations (Fig. 6), our model AE_RTM_corr shows more consistent and clearer patterns for some variables (Fig. 6). For example, understory plant growth (LAI_u) declines from April due to reduced light penetration from increasing canopy growth (LAI); coniferous forests exhibit different patterns than deciduous forests, with higher fractional coverage (fc) and less variation over time, as would be expected. NNRegressor temporal variations appear to be less consistent (see Fig. A.6).

We have clustered the 7 inferred variables by species and calculated the Jeffreys-Matusita (JM) distance to assess the separability of the 12 species based on these variables (refer to Tab. A.3 and Tab. A.4 for detailed statistics). The JM distance, which varies between 0 and 2, serves as an indicator of separability, with higher values denoting greater distinction between two distributions. Consequently, we computed the pairwise JM distances for the species represented by the seven biophysical variables. This quantifies the effectiveness of our model in differentiating the species. As shown in Fig. 7, our model achieves clear separation between species of different forest types and shows improved separability for species within the same forest type, indicating that the model is capable of inferring variables with clearer distinguishing power within the latent space.

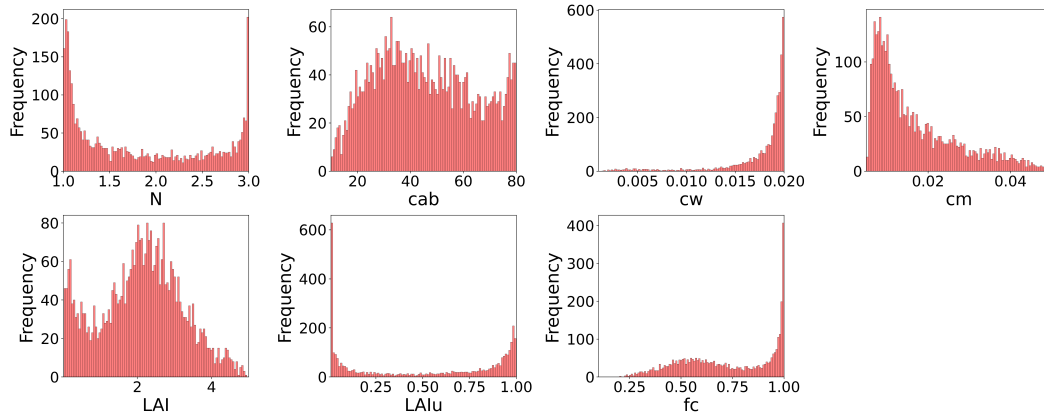


(a) NNRegressor: $X_{r,D}$ v. X_r

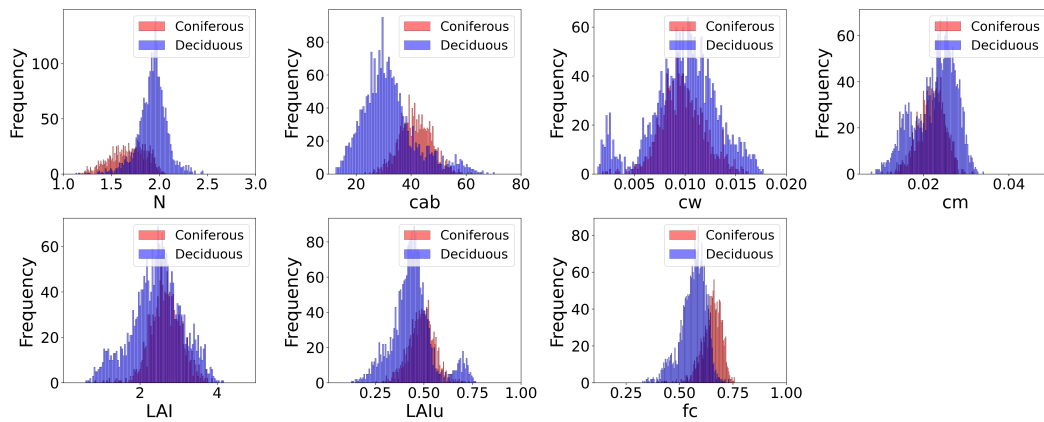


(b) AE_RTM_corr: $X_{r,C}$ v. X_r

Figure 3: **Superior reconstruction accuracy for AE_RTM_corr**, illustrated by spectral band. (a) Reconstruction from NNRegressor displays clear bias (b) AE_RTM_corr reconstructs X_r markedly more accurately.



(a) NNRegressor: $Z_{r,D}$



(b) AE_RTM_corr: $Z_{r,C}$

Figure 4: **Distributions of variables.** (a) Application of the NNRegressor to real Sentinel-2 spectra leads to implausible parameter distributions that tend to break out of the preset parameter ranges. (b) Distributions of variables learned by AE_RTM_corr are plausible and distinguish between forest types.

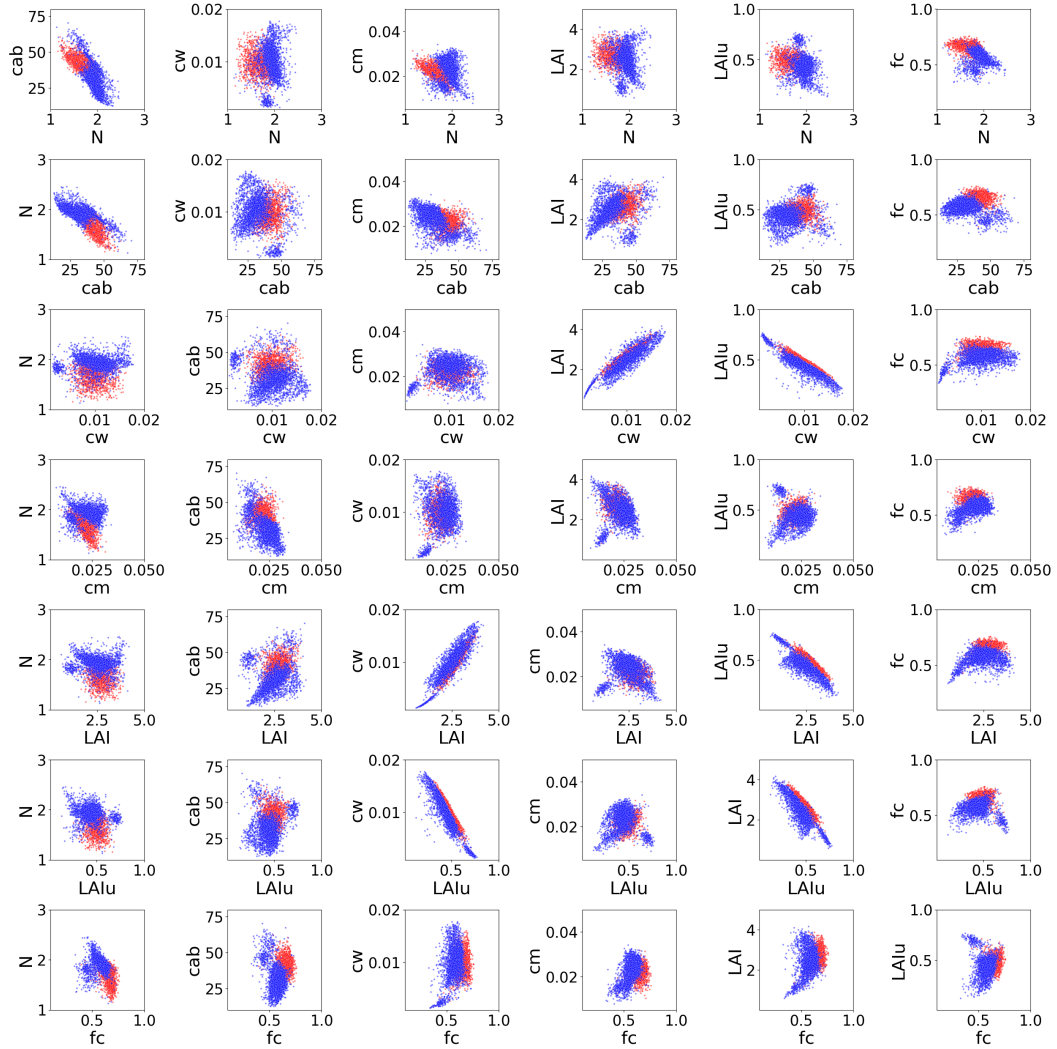


Figure 5: **Pairwise co-distributions of $Z_{r,C}$ learned by AE-RTM-corr.** Red: coniferous forest. Blue: deciduous forest. Our model can learn distinct physical patterns.

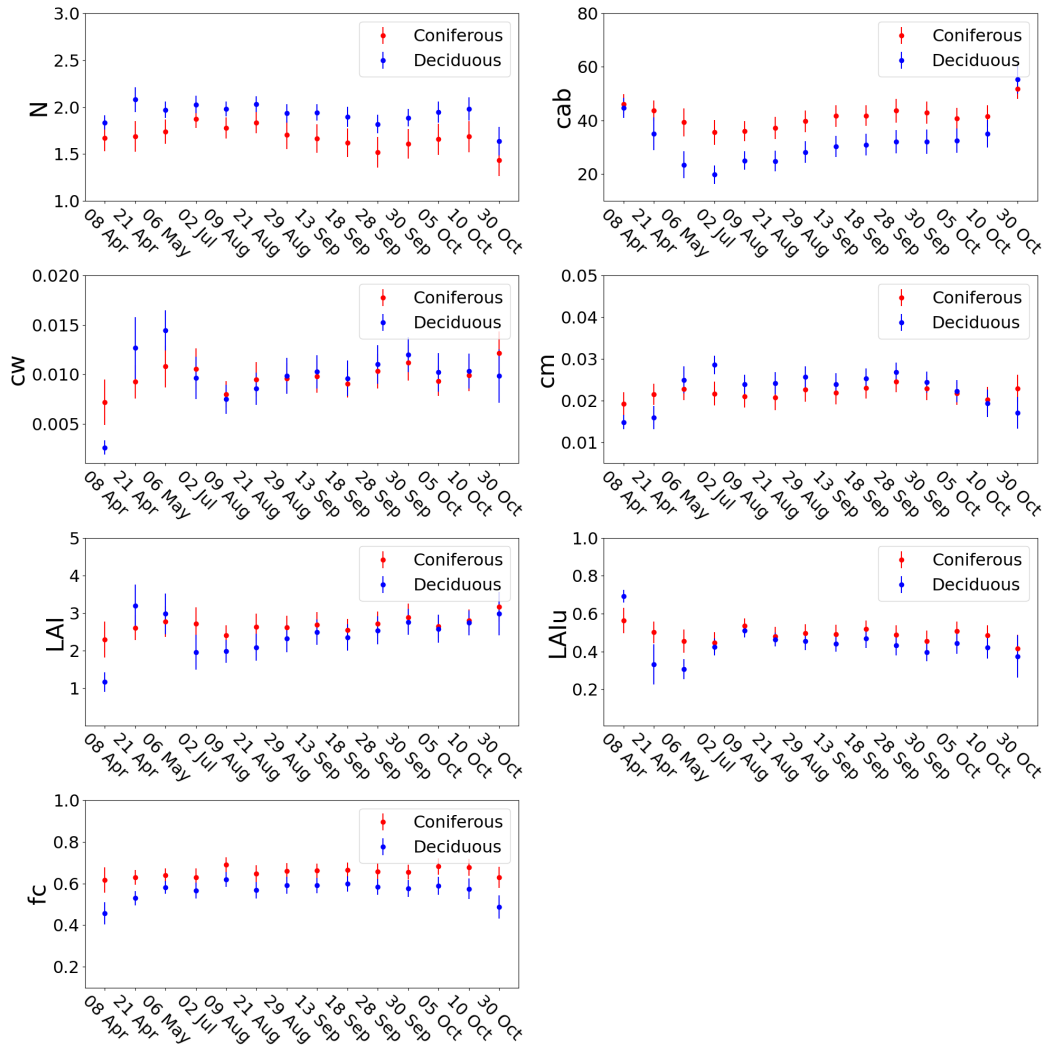


Figure 6: **Temporal variations of inferred physical parameters $Z_{r,C}$.** *AE-RTM_corr* effectively captures distinct, temporally smooth and plausible variations for different forest types.

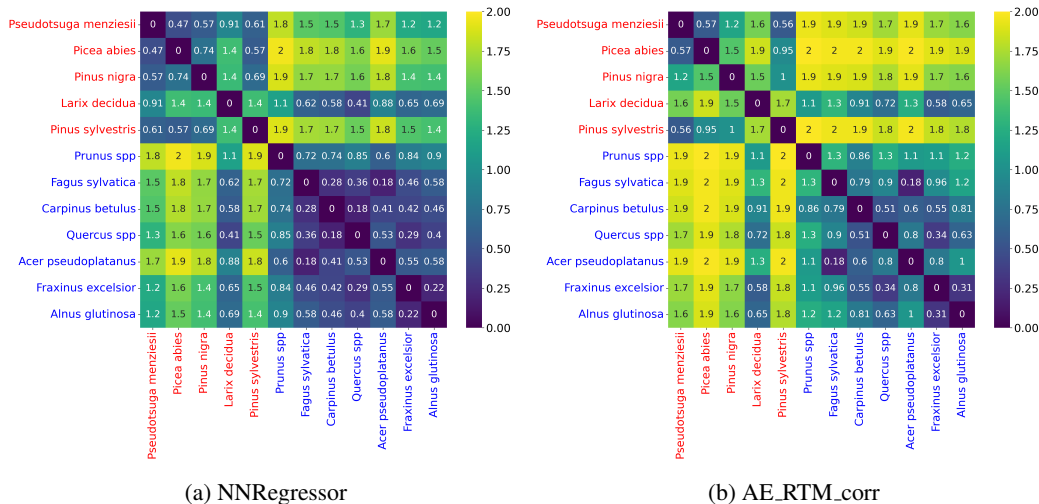


Figure 7: **Pairwise Jeffreys-Matusita (JM) distance between species** based on the learned variables. *Red: coniferous species. Blue: deciduous species. JM distance is a statistical measure used to quantify the separability between two probability distributions. Our model is able to learn more disentangled variables within the latent space.*

4.3 ABLATION STUDIES

To evaluate the effects of our experimental design, we have conducted ablation studies (Tab. 4). The systematic bias of the RTM can be observed by comparing the MSE of the classical auto-encoder ($\mathbf{E}_A+\mathbf{D}_A$) with that of one where the decoder has been replaced by the RTM ($\mathbf{E}_B+\mathbf{F}$). In this comparison, the reconstruction accuracy becomes significantly worse—more than an order of magnitude—when the decoder is replaced by the RTM. However, with bias correction, our model achieves MSE losses comparable to those of the classical encoder.

The effects of bias correction extend beyond improving reconstruction accuracy; they also enhance the learning of variables in the latent space. Comparing the retrieved variables of our model with and without the bias correction layer (Fig. 8), it is evident that the RTM’s bias distorts the distribution of several variables to extremes, likely in an attempt to minimize the reconstruction loss despite the presence of bias. In contrast, with bias correction, our model learns more plausible distributions of the variables.

Table 4: **MSE loss of models under different steps of the inversion.** *The MSE loss of our final model is more than one magnitude lower than the one without bias correction, and is comparable to the classical auto-encoder.*

Model	Ablation	Dataset	MSE_{train}	MSE_{val}	MSE_{test}
$\mathbf{E}_A+\mathbf{D}_A$	w/o RTM, w/o correction	D_r	0.0193	0.0219	0.0191
$\mathbf{E}_B+\mathbf{F}$	w/ RTM, w/o correction	D_r	0.0875	0.0833	0.0856
$\mathbf{E}_C+\mathbf{F}+\mathbf{C}_C$ (ours)	w/ RTM, w/ correction	D_r	0.0210	0.0235	0.0217

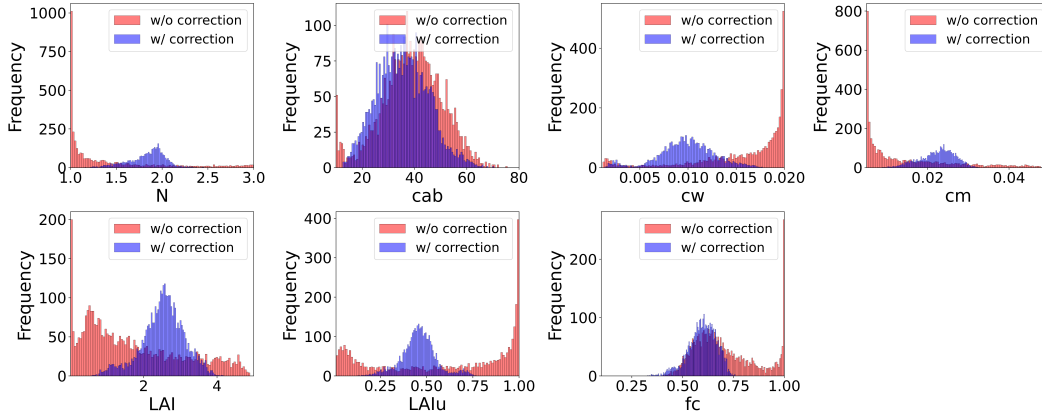


Figure 8: **Distributions of variables** from our model before and after bias correction ($Z_{r,B}$ v. $Z_{r,C}$). Without bias correction the variable distributions (red) are implausible, tending to break out beyond the preset bounded ranges. With bias correction (blue), the model is able to learn more plausible distributions.

5 CONCLUSION

We have developed an end-to-end method for extracting biophysical variables from satellite spectra. We integrated a complex radiative transfer model with modern machine learning, using auto-encoder learning to invert a physical model and correct its biases. Our extensive analysis shows markedly improved reconstruction loss, and strongly suggests that recovered physical variables are more plausible than previous methods. There may also be broader implications for methodology in physics-informed machine learning.

Acknowledgement: This work was supported by the UKRI Centre for Doctoral Training in Application of Artificial Intelligence to the study of Environmental Risks (reference EP/S022961/1) and Cambridge Centre for Carbon Credits. We would also like to thank Markus Immitzer from Mantle Labs for having shared the Sentinel-2 data with us.

REFERENCES

- Clement Atzberger. Development of an invertible forest reflectance model: The infor-model. In *A decade of trans-european remote sensing cooperation. Proceedings of the 20th EARSeL Symposium Dresden, Germany*, volume 14, pp. 39–44, 2000.
- Xi Chen, Yan Duan, Rein Houthoofd, John Schulman, Ilya Sutskever, and Pieter Abbeel. Info-gan: Interpretable representation learning by information maximizing generative adversarial nets. *Advances in neural information processing systems*, 29, 2016.
- Martin Claverie, Junchang Ju, Jeffrey G Masek, Jennifer L Dungan, Eric F Vermote, Jean-Claude Roger, Sergii V Skakun, and Christopher Justice. The harmonized landsat and sentinel-2 surface reflectance data set. *Remote sensing of environment*, 219:145–161, 2018.
- B Combal, Frédéric Baret, M Weiss, Alain Trubuil, D Mace, A Pragnere, R Myneni, Y Knyazikhin, and L Wang. Retrieval of canopy biophysical variables from bidirectional reflectance: Using prior information to solve the ill-posed inverse problem. *Remote sensing of environment*, 84(1):1–15, 2003.
- Timothy F Cootes, Christopher J Taylor, David H Cooper, and Jim Graham. Active shape models—their training and application. *Computer vision and image understanding*, 61(1):38–59, 1995.
- Cian Eastwood and Christopher KI Williams. A framework for the quantitative evaluation of disentangled representations. In *International Conference on Learning Representations*, 2018.
- Jean-Philippe Gastellu-Etchegorry, Valérie Demarez, Veronique Pinel, and Francis Zagolski. Modeling radiative transfer in heterogeneous 3-d vegetation canopies. *Remote sensing of environment*, 58(2):131–156, 1996.
- Narendra S Goel. Models of vegetation canopy reflectance and their use in estimation of biophysical parameters from reflectance data. *Remote sensing reviews*, 4(1):1–212, 1988.
- P Gong. Inverting a canopy reflectance model using a neural network. *International Journal of Remote Sensing*, 20(1):111–122, 1999.
- Ian Goodfellow, Jean Pouget-Abadie, Mehdi Mirza, Bing Xu, David Warde-Farley, Sherjil Ozair, Aaron Courville, and Yoshua Bengio. Generative adversarial networks. *Communications of the ACM*, 63(11):139–144, 2020.
- Zhongkai Hao, Songming Liu, Yichi Zhang, Chengyang Ying, Yao Feng, Hang Su, and Jun Zhu. Physics-informed machine learning: A survey on problems, methods and applications. *arXiv preprint arXiv:2211.08064*, 2022.
- Irina Higgins, Loic Matthey, Arka Pal, Christopher Burgess, Xavier Glorot, Matthew Botvinick, Shakir Mohamed, and Alexander Lerchner. beta-vae: Learning basic visual concepts with a constrained variational framework. In *International conference on learning representations*, 2017.
- Tommaso Jucker, John Caspersen, Jérôme Chave, Cécile Antin, Nicolas Barbier, Frans Bongers, Michele Dalponte, Karin Y van Ewijk, David I Forrester, Matthias Haeni, et al. Allometric equations for integrating remote sensing imagery into forest monitoring programmes. *Global change biology*, 23(1):177–190, 2017.
- Tero Karras, Samuli Laine, and Timo Aila. A style-based generator architecture for generative adversarial networks. In *Proceedings of the IEEE/CVF conference on computer vision and pattern recognition*, pp. 4401–4410, 2019.
- Diederik P Kingma and Max Welling. Auto-encoding variational bayes. *arXiv preprint arXiv:1312.6114*, 2013.
- Abhishek Kumar, Prasanna Sattigeri, and Avinash Balakrishnan. Variational inference of disentangled latent concepts from unlabeled observations, 2018.
- Xiaowen Li and Alan H Strahler. Geometric-optical modeling of a conifer forest canopy. *IEEE Transactions on Geoscience and Remote Sensing*, (5):705–721, 1985.

-
- Francesco Locatello, Stefan Bauer, Mario Lucic, Gunnar Rätsch, Sylvain Gelly, Bernhard Schölkopf, and Olivier Bachem. Challenging common assumptions in the unsupervised learning of disentangled representations, 2019.
- Matthew M Loper and Michael J Black. Opendr: An approximate differentiable renderer. In *Computer Vision–ECCV 2014: 13th European Conference, Zurich, Switzerland, September 6–12, 2014, Proceedings, Part VII 13*, pp. 154–169. Springer, 2014.
- Peter Y Lu, Samuel Kim, and Marin Soljačić. Extracting interpretable physical parameters from spatiotemporal systems using unsupervised learning. *Physical Review X*, 10(3):031056, 2020.
- OpenAI. Gpt-4 technical report, 2023.
- A Rosema, W Verhoef, H Noorbergen, and JJ Borgesius. A new forest light interaction model in support of forest monitoring. *Remote Sensing of Environment*, 42(1):23–41, 1992.
- Martin Schlerf and Clement Atzberger. Inversion of a forest reflectance model to estimate structural canopy variables from hyperspectral remote sensing data. *Remote sensing of environment*, 100(3):281–294, 2006.
- Gwynn H Suits. The calculation of the directional reflectance of a vegetative canopy. *Remote Sensing of Environment*, 2:117–125, 1971.
- I Thompson, B Mackey, S McNulty, A Mosseler, et al. Forest resilience, biodiversity, and climate change. In *A synthesis of the biodiversity/resilience/stability relationship in forest ecosystems. Secretariat of the Convention on Biological Diversity, Montreal. Technical Series*, volume 43, pp. 1–67, 2009.
- J-L Widlowski, B Pinty, M Lopatka, C Atzberger, D Buzica, Michaël Chelle, M Disney, J-P Gastellu-Etchegorry, M Gerboles, N Gobron, et al. The fourth radiation transfer model inter-comparison (rami-iv): Proficiency testing of canopy reflectance models with iso-13528. *Journal of Geophysical Research: Atmospheres*, 118(13):6869–6890, 2013.
- Yoël Zérah, Silvia Valero, and Jordi Inglada. Physics-guided interpretable probabilistic representation learning for high resolution image time series. *IEEE Transactions on Geoscience and Remote Sensing*, 2022.
- Yoël Zérah, Silvia Valero, and Jordi Inglada. Physics-constrained deep learning for biophysical parameter retrieval from sentinel-2 images: inversion of the prosail model. *Available at SSRN 4671923*, 2023.

A APPENDIX

A.1 CONVERSION OF INFORM TO PYTORCH ASSISTED BY GPT-4

The original modules of INFORM are extracted from a vegetation app called EnMap¹. It is implemented using Numpy arrays and operations. However, to track the computational graph and enable gradient backpropagation, it needs to be reimplemented using PyTorch operations. However, INFORM is a complicated physical model, and reimplementing it in PyTorch manually seems challenging. In light of the recent development of large language models, we decide to utilize GPT-4 (OpenAI, 2023) to assist in the conversion from NumPy to PyTorch. While GPT-4 has helped us cut out a significant amount of repetitive work, it is worth mentioning a few of its limitations:

GPT-4 is useful for converting commonly seen operations from NumPy into PyTorch. With its assistance, we have successfully converted 1,742 lines of code across various scripts from the original implementation to PyTorch (e.g. Listing 1 and Listing 2). However, some operations e.g. the exponential integral function², has no equivalent in PyTorch (Listing 2). To calculate their derivative, we will still need to implement our own `backward` functions to define derivatives.

Additionally, GPT-4 only accepts text input of limited length, which means it can only convert a script snippet piece by piece. As the conversation lengthens, it may make mistakes. For instance, it converts `numpy.radians` to `torch.radians`, which does not exist in PyTorch. Thus it is still important to visually check the conversion, run unit tests, and work on compiling all the scripts together. Interestingly, GPT allows for prompt engineering, which means we can provide feedback to refine its conversions, such as requesting it to highlight uncertain parts for review in subsequent conversions.

```
1 n = PD_refractive
2 k = (np.outer(Cab, PD_k_Cab) + np.outer(Car, PD_k_Car) + np.outer(Anth,
   PD_k_Anth) +
3     np.outer(Cbrown, PD_k_Brown) + np.outer(Cw, PD_k_Cw) + np.outer(Cm,
   PD_k_Cm)) / N[:, np.newaxis]
4
5 ind_k0_row, ind_k0_col = np.where(k == 0)
6
7 if len(ind_k0_row) > 0:
8     k[ind_k0_row, ind_k0_col] = np.finfo(float).eps
9 trans = (1 - k) * np.exp(-k) + (k ** 2) * expl(k)
```

Listing 1: Example code of F initially implemented using NumPy. *It features an exponential integral function 'expl' in line 9. Additionally, it's important to highlight that in line 3, the structure parameter N functions as a denominator in the calculation, therefore, it cannot be zero.*

```
1 n = PD_refractive
2 k = (torch.outer(Cab, PD_k_Cab) + torch.outer(Car, PD_k_Car) + torch.
   outer(Anth, PD_k_Anth) +
3     torch.outer(Cbrown, PD_k_Brown) + torch.outer(Cw, PD_k_Cw) + torch.
   outer(Cm, PD_k_Cm)) / N.unsqueeze(-1)
4
5 ind_k0_row, ind_k0_col = torch.where(k == 0)
6
7 if len(ind_k0_row) > 0:
8     k[ind_k0_row, ind_k0_col] = torch.finfo(float).eps
9 trans = (1 - k) * torch.exp(-k) + (k ** 2) * torch.from_numpy(expl(k.
   numpy()))
```

Listing 2: Conversion of F to PyTorch by GPT. *It is followed by feedback on expl to raise user's attention. Here is an excerpt: "Please note that the expl function is not available in PyTorch as of my last training cut-off in September 2021. We can import it from the scipy.special library, but we have to convert the tensor to numpy before using it and convert the result back to a tensor. It's not ideal in terms of performance, but I'm afraid there's no other option for now. Please check if there is an updated version of PyTorch that includes this function."*

¹EnMap

²`scipy.special.expl`

Note that this experiment was done in May, 2023, when GPT-4 was still in its early phase and has several features updated since then. For instance, it now can accept longer text inputs. Nonetheless, we believe the limitations discussed above still largely hold true and are worth considering for similar tasks in the future.

A.2 VALIDATING THE PYTORCH IMPLEMENTATION OF INFORM

To validate the implementation of INFORM in PyTorch against its original version in Numpy, before generating D_s , we randomly sample 10,000 sets of variables, passed them through each implementation, and compare their outputs (Tab. A.1). The mismatch rate of the outputs is 0.457% when the absolute tolerance is set to 1e-5. The maximum absolute difference over all 130000 output reflectances from the two implementations is 3.050e-5 wherein the physical unit of reflectance here is 1. This indicates that INFORM implemented in PyTorch is substantially equivalent to its original version, therefore can be used in subsequent tasks.

Table A.1: **Unit test of the outputs of our PyTorch implementation of F against the original NumPy version.** *The total number of elements to compare is 130000 as we simulate the same set of 10000 samples for both implementations, each with 13 spectral bands of Sentinel-2.*

Total Elements	Mismatched Elements	Absolute Tolerance	Mismatch Ratio	Max Absolute Difference
130000	594	1e-5	0.457%	3.050e-5

A.3 INTEGRATING INFORM INTO MACHINE LEARNING

A.3.1 NUMERICAL INSTABILITY OF INFORM

With INFORM now implemented in PyTorch, we can backpropagate gradients through this physical model. However, the model is sensitive to input variable ranges and is non-differentiable at certain points. Furthermore, complex operations like exponential, logarithm, and square root, often lead to numerical instability during derivative computation, even though these operations are theoretically differentiable. To solve these issues, we have developed specific methods to stabilize the training when INFORM is used.

A.3.2 FORWARD PASS

The input variables Z of INFORM are non-negative values with physical meanings (Tab. 1). In practice, INFORM can fail in the forward pass when Z from other value ranges are provided. Thus we choose to infer a normalised variable Λ ranging from 0 to 1 for each biophysical variable; then we map Λ to each biophysical variable in its original scale using the value ranges provided in Tab. 1 (eq. (5)). This not only enables a successful forward pass of INFORM but also narrows down the search space for optimization.

$$Z = (Max - Min) \cdot \Lambda + Min \quad (5)$$

A.3.3 BACKPROPAGATION

Despite a successful forward pass, the backpropagation, however, remains unstable. For successful learning, it is necessary to backpropagate gradients through the physical model i.e. INFORM in our case. The aforementioned caveats of INFORM however have resulted in backpropagation failures, leading to NaN gradient and then NaN loss. During experiments to stabilize the backpropagation, we notice that NaN gradients, when they initially appear, are always in association with specific sets of INFORM variables. Ideally, one would apply constraints to specific INFORM operations causing these NaN gradients. However, working out such constraints seems challenging unless we understand INFORM and its differentiability thoroughly.

In response to this, we introduce a simple workaround: since it is NaN gradients that cause the subsequent learning failure, we replace them with a small random value, which is sampled from a

uniform distribution ranging from 0 to 1 and subsequently scaled by $1e-7$, whenever these gradients first appear. The specific workflow of the algorithm is described in algorithm 1

Algorithm 1 Gradient stabilization

```

Calculate gradients
Initialize list grads, containing gradients of all model parameters where gradients exist and contain any NaN values
if grads is not empty then
  Set a small constant epsilon equal to  $1e-7$ 
  for each v in grads do
    Generate random values of the same shape as v, scaled by epsilon
    Create a mask where v is NaN or equals 0
    Replace values in v where the mask is True with corresponding random values
  end for
end if
Update gradients

```

A.3.4 STABILIZED TRAINING PROCESS

Our method has effectively stabilized the learning of E_B and E_C in the autoencoder framework, despite instability of F during backpropagation. As can be seen in Fig. A.1, both training and validation losses of AE_RTM_corr keep converging over epochs. Therefore, by preventing the propagation of NaN gradients to earlier layers and allowing the normal progression of the forward pass, the stabilizer has effectively enabled the training process to bypass instability points in the optimization space and allowed a continuous search for optimal points.

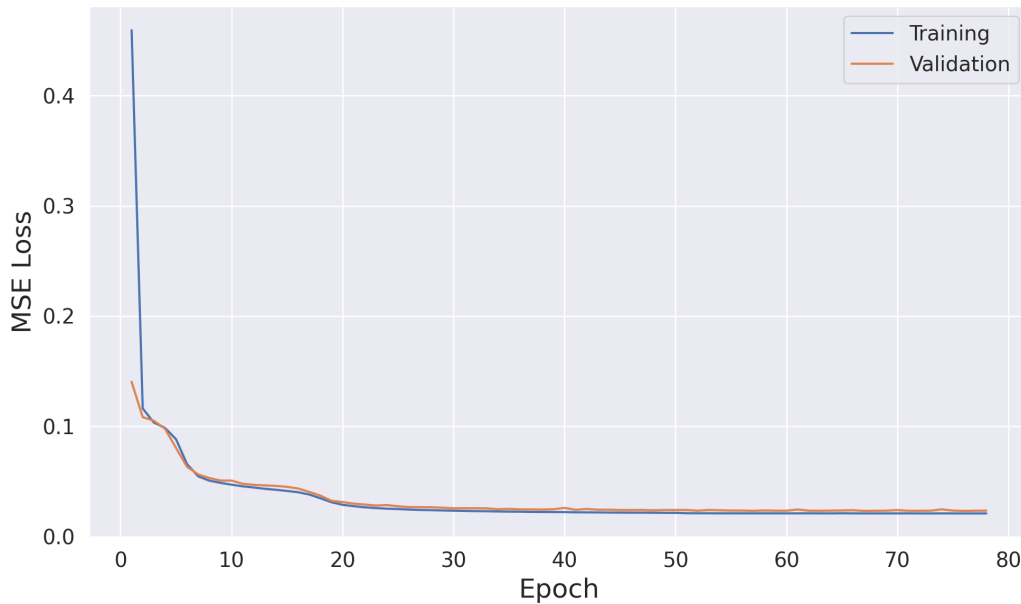


Figure A.1: **Training and validation losses of AE_RTM_corr.** Our strategy to update the gradients has overcome the instability of F during backpropagation and allowed the convergence of training loss.

A.4 BIOPHYSICAL VARIABLES OF INFORM

The input of INFORM consists of biophysical variables of three hierarchical levels. Note that the original INFORM does not have fractional coverage fc as an input variable. We include fc as one

of the seven variables to be learned directly by \mathbf{E} , which will be used to infer crown diameter cd and height h based on derived equations. As the fractional coverage is jointly defined by the stem density and crown diameter within each unit hectare (or $10,000 m^2$), cd can be derived given fc and sd using eq. (6). Furthermore, to derive h , we fit an allometric equation (eq. (7)) using the samples of temperate forests from the global allometric database (Jucker et al., 2017). R^2 of the derived equation between h and cd eq. (7) is 0.383.

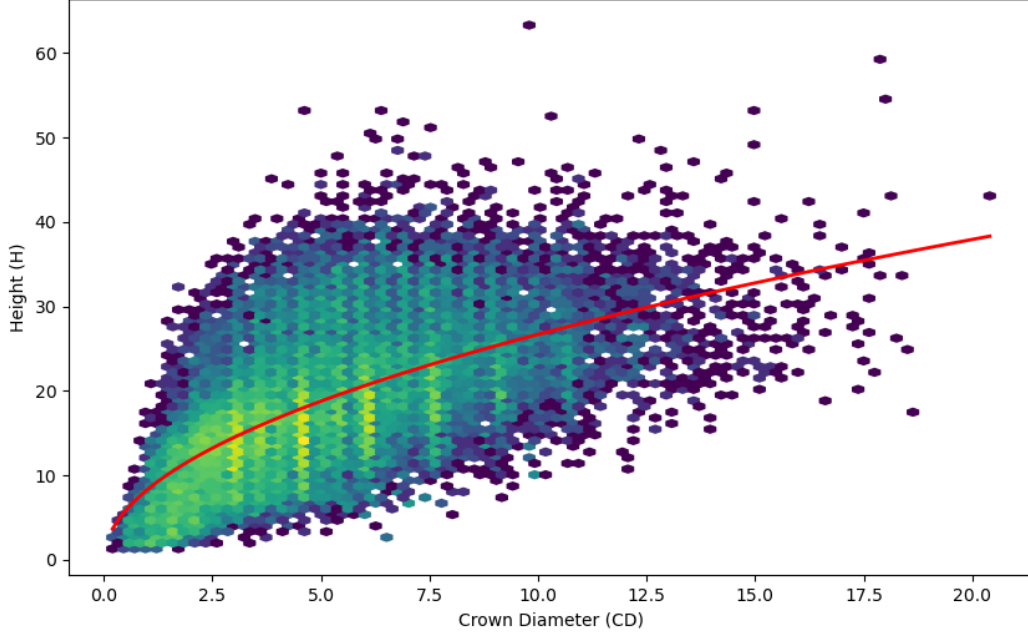


Figure A.2: **Allometric relationship between h and cd .** We fit an allometric equation between h and cd (eq. (7)). R^2 of the fitted equation is 0.383.

$$cd = 2 \cdot \sqrt{\frac{fc \cdot 10000}{\pi \cdot sd}} \quad (6)$$

$$h = \exp(2.117 + 0.507 \cdot \ln(cd)) \quad (7)$$

A.5 TEMPORAL AND SPECIES INFORMATION OF THE REAL DATASET

Statistics of the D_r can be viewed in Tab. A.2. These spectra were sampled from individual sites covering a time sequence of 14 timestamps. Note that our current training strategy does not integrate temporal information into the inferencing process, although temporal variations are evaluated. Such temporal information could serve as useful prior knowledge to boost the model’s performance, especially to ensure the consistency of temporal variations, which we will consider in future works. All these samples cover both coniferous and deciduous forests consisting of 5 and 7 species, respectively:

- **Coniferous forest:** Pseudotsuga Menziesii, Picea Abies, Pinus Nigra, Larix Decidua, Pinus Sylvestris.
- **Deciduous forest:** Prunus Spp, Fagus Sylvatica, Carpinus Betulus’, Quercus Spp, Acer Pseudoplatanus, Fraxinus Excelsior’, Alnus Glutinosa.

Table A.2: Statistics of the real dataset

Total Number of Spectra	Number of Individual Sites	Number of Dates	Number of Species
17962	1283	14	12

A.6 BIAS CORRECTION

Without bias correction, our model struggles to accurately reconstruct the input bands (Fig. A.3), displaying reconstruction patterns akin to the baseline. Specifically, for the visible bands, the model tends to overestimate values at lower ranges. In the case of near-infrared bands, it tends to underestimate at higher ranges, whereas the bias in the shortwave band is less pronounced. The biases identified by our model (Fig. A.4) exhibit temporally consistent and smooth patterns, mirroring the temporal variations observed in the variables. As revealed by the histogram of biases (Fig. 2), the spectral signatures simulated by the original RTM and our AE_RTM_corr, for the same set of retrieved variables, also reflect the tendency of the RTM to overestimate for coniferous and underestimate for deciduous species, respectively (Fig. A.5).

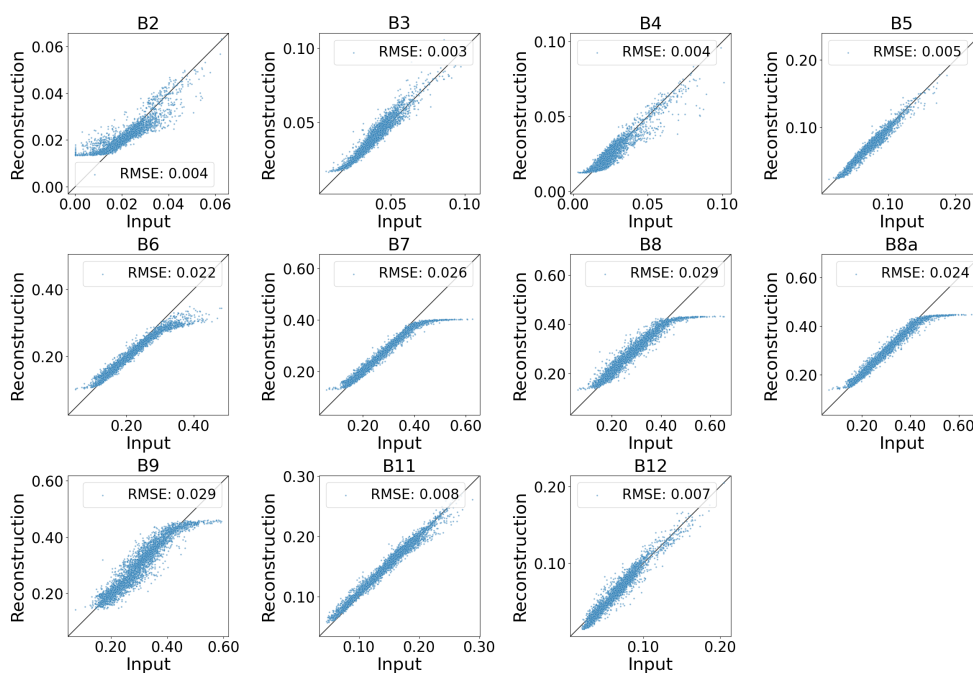


Figure A.3: **Reconstruction visualization of our model without bias correction (X_r against $X_{r,B}$).** Without the correction by C_C , $X_{r,B}$ also shows bias with similar patterns as $NNRegressor$.

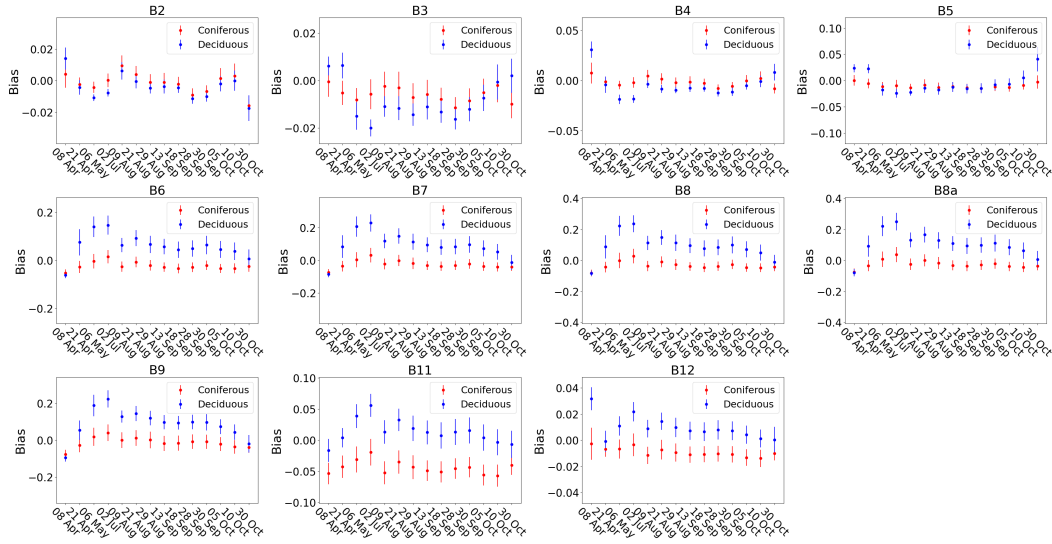


Figure A.4: **Temporal variations of biases learned by AE_RTM_corr.** Biases from the same spectral group, e.g. those in the near-infrared, display similar patterns, which are also distinct between forest types.

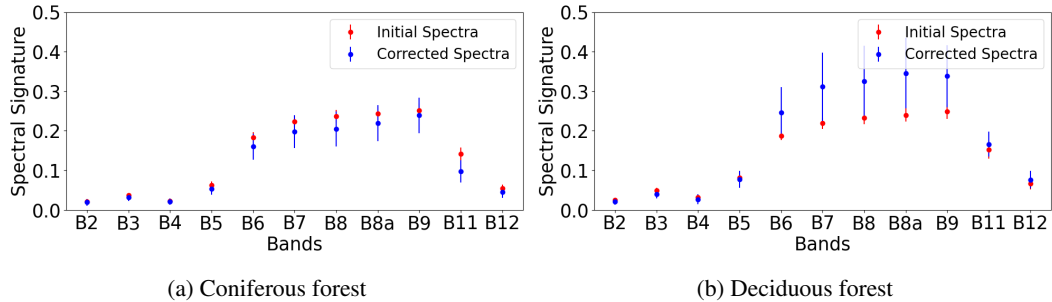


Figure A.5: **Spectral signature** before and after bias correction. The RTM tends to over-estimate the spectra for coniferous forest and under-estimate for deciduous forest.

A.7 BIOPHYSICAL VARIABLES

The baseline model’s learning of temporal variations in variables demonstrates increased variability over time, often reaching extreme values at the boundaries of specified ranges (Fig. A.6). Additionally, we have presented tables summarizing the means and standard deviations of the learned variables, categorized by species as identified by the baseline (Tab. A.3) and by our model (Tab. A.4). Our analysis, particularly of the Jeffreys-Matusita distance of species distributions based on learned variables (Fig. 7), indicates that our model succeeds in learning variables with more distinguishing power within the latent space.

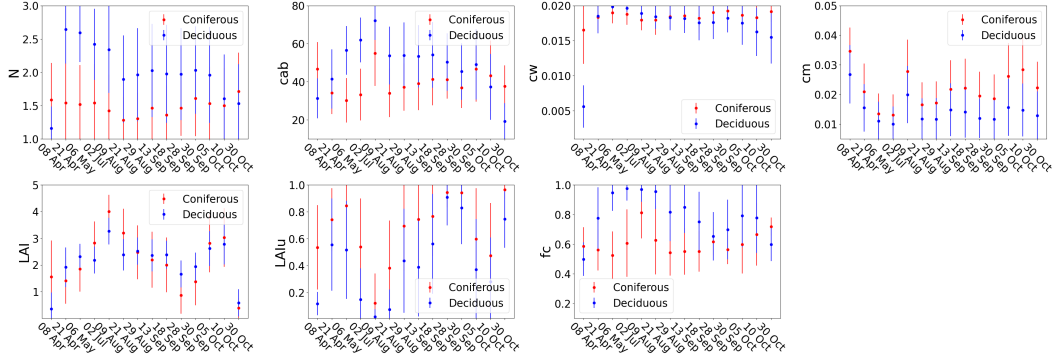


Figure A.6: **Temporal variation of the $Z_{r,D}$ learned by NNRegressor, clustered by forest types. Compared to our model, the temporal variations of the variables retrieved by the baseline model are less consistent over time.**

Table A.3: **Statistics of $Z_{r,D}$ learned by NNRegressor**

Species	N	cab	cw	cm	LAI	LAIu	fc
Pseudotsuga menziesii	1.43 ± 0.54	38.31 ± 14.87	1.79 ± 0.25	1.91 ± 1.02	2.15 ± 1.24	0.72 ± 0.34	0.61 ± 0.19
Picea abies	1.36 ± 0.44	39.49 ± 13.24	1.87 ± 0.17	2.15 ± 0.98	1.72 ± 1.25	0.84 ± 0.25	0.58 ± 0.13
Pinus nigra	1.56 ± 0.55	39.50 ± 15.81	1.86 ± 0.20	2.47 ± 1.13	2.32 ± 1.42	0.54 ± 0.37	0.62 ± 0.19
Larix decidua	1.50 ± 0.50	38.26 ± 13.85	1.61 ± 0.42	1.43 ± 0.69	1.90 ± 1.04	0.56 ± 0.40	0.67 ± 0.21
Pinus sylvestris	1.56 ± 0.58	42.34 ± 15.68	1.90 ± 0.11	1.99 ± 1.01	2.40 ± 1.25	0.67 ± 0.37	0.59 ± 0.18
Prunus spp	1.90 ± 0.84	43.22 ± 22.17	1.35 ± 0.57	1.60 ± 1.04	1.79 ± 0.82	0.46 ± 0.34	0.71 ± 0.25
Fagus sylvatica	1.98 ± 0.76	46.75 ± 20.22	1.71 ± 0.42	1.21 ± 0.79	2.17 ± 0.92	0.33 ± 0.37	0.82 ± 0.23
Carpinus betulus	1.96 ± 0.71	47.55 ± 19.40	1.67 ± 0.36	1.36 ± 0.84	1.91 ± 0.91	0.55 ± 0.40	0.75 ± 0.21
Quercus spp	1.91 ± 0.69	48.59 ± 18.28	1.73 ± 0.41	1.46 ± 0.83	2.09 ± 0.94	0.55 ± 0.40	0.75 ± 0.21
Acer pseudoplatanus	2.21 ± 0.75	51.34 ± 20.31	1.72 ± 0.45	1.51 ± 0.79	2.01 ± 0.99	0.27 ± 0.33	0.86 ± 0.18
Fraxinus excelsior	2.16 ± 0.71	51.67 ± 18.05	1.76 ± 0.37	1.93 ± 1.17	2.05 ± 1.07	0.44 ± 0.39	0.78 ± 0.21
Alnus glutinosa	2.22 ± 0.72	55.01 ± 18.09	1.78 ± 0.34	2.03 ± 0.97	2.04 ± 1.03	0.46 ± 0.41	0.76 ± 0.20

Table A.4: **Statistics of $Z_{r,C}$ learned by AE-RTM_corr**

Species	N	cab	cw	cm	LAI	LAIu	fc
Pseudotsuga menziesii	1.65 ± 0.16	39.96 ± 5.33	1.00 ± 0.24	2.36 ± 0.23	2.66 ± 0.43	0.49 ± 0.07	0.66 ± 0.04
Picea abies	1.53 ± 0.16	43.33 ± 4.89	0.99 ± 0.24	2.37 ± 0.21	2.70 ± 0.43	0.50 ± 0.07	0.68 ± 0.04
Pinus nigra	1.75 ± 0.16	42.71 ± 5.63	0.96 ± 0.19	1.97 ± 0.28	2.73 ± 0.37	0.48 ± 0.06	0.64 ± 0.04
Larix decidua	1.86 ± 0.13	36.52 ± 7.50	0.88 ± 0.25	2.28 ± 0.33	2.34 ± 0.48	0.49 ± 0.08	0.59 ± 0.05
Pinus sylvestris	1.71 ± 0.14	39.87 ± 5.18	0.99 ± 0.18	2.24 ± 0.24	2.68 ± 0.34	0.48 ± 0.05	0.66 ± 0.03
Prunus spp	1.93 ± 0.12	34.71 ± 8.65	0.80 ± 0.30	2.26 ± 0.37	2.13 ± 0.54	0.50 ± 0.10	0.53 ± 0.05
Fagus sylvatica	1.98 ± 0.17	29.76 ± 10.71	0.94 ± 0.33	2.24 ± 0.53	2.32 ± 0.69	0.43 ± 0.11	0.54 ± 0.06
Carpinus betulus	1.90 ± 0.11	33.38 ± 9.65	0.99 ± 0.31	2.37 ± 0.48	2.42 ± 0.61	0.45 ± 0.10	0.56 ± 0.05
Quercus spp	1.87 ± 0.11	33.46 ± 8.55	1.06 ± 0.33	2.35 ± 0.48	2.56 ± 0.63	0.44 ± 0.10	0.59 ± 0.06
Acer pseudoplatanus	1.99 ± 0.14	30.82 ± 10.09	0.99 ± 0.34	2.12 ± 0.49	2.45 ± 0.68	0.42 ± 0.12	0.54 ± 0.05
Fraxinus excelsior	1.90 ± 0.12	34.73 ± 8.27	1.02 ± 0.32	2.19 ± 0.39	2.57 ± 0.56	0.45 ± 0.10	0.58 ± 0.05
Alnus glutinosa	1.89 ± 0.13	35.02 ± 8.37	0.99 ± 0.27	2.22 ± 0.30	2.52 ± 0.48	0.46 ± 0.08	0.59 ± 0.05